Powder Technology 396 (2022) 210–223

Contents lists available at ScienceDirect

Powder Technology

journal homepage: www.elsevier.com/locate/powtec

Mixing and dispersion behaviours of ellipsoid particles in a bubbling fluidized bed

Shiliang Yang [a], Site Hu [b], Wentao Zhang [b,c,*]

[a] State Key Laboratory of Complex Nonferrous Metal Resources Clean Utilization, Kunming University of Science and Technology, Kunming 650093, Yunnan, China
[b] Midea Corporate Research Center, Foshan 528311, Guangdong, China
[c] Key Laboratory for Mechanics in Fluid Solid Coupling Systems, Institute of Mechanics, Chinese Academy of Sciences, Beijing 100190, China

ARTICLE INFO

Article history:
Received 30 July 2021
Received in revised form 21 August 2021
Accepted 20 October 2021
Available online 23 October 2021

Keywords:
Non-spherical particles
Discrete element method
Solid mixing
Solid dispersion
Fluidized bed

ABSTRACT

Fluidization of non-spherical particles is widely practised in chemical engineering processes. In this work, the mixing and dispersion behaviours of non-spherical particles in a bubbling fluidized bed (BFB) are explored by a computational fluid dynamics-discrete element method (CFD-DEM) featuring a super-quadric model to describe particle morphology. After model validation, the general flow patterns, solid mixing, and solid dispersion of ellipsoid particles are studied, together with the discussion of the effect of aspect ratio (AR) on fluidization behaviours. The results show that minimum fluidization velocity increases with the aspect ratio. Bed permeability depends on bed porosity and particle shape. Bubbles place a significant role in determining flow patterns, which induce a double-recirculation pattern where particles mainly move from the wall region to the central region in the lower bed and oppositely in the upper bed. Ellipsoid particles with higher sphericity (e.g., AR = 0.75 and 1.5) show a smaller mixing index in the bed. The magnitudes of solid dispersion coefficients in x, y, and z directions are about ~10^{-3} m^2/s, ~10^{-5} m^2/s, and ~ 10^{-2} m^2/s, respectively. Ellipsoid particles with higher sphericity show larger solid dispersion intensity. These findings shed light on the fundamental understanding of the particle shape on fluidization dynamics.

1. Introduction

Fluidization of particles has been widely practised in chemical engineering processes, such as catalysis, pyrolysis, gasification, granulation, and drying [1–3], in which gas-solid mixing property plays an important role in determining heat and mass transfer, and the resulting reaction performance [4]. Thus, understanding solid mixing during fluidization is of significance to the design, operation, and optimization of fluidized beds [5]. In the past decades, great experimental efforts have been made to explore the solid mixing together with flow dynamics, bubble evolution, and pressure drop using magnetic particle tracking (MPT) and Particle Image Velocimetry (PIV) [6,7]. However, the establishment of the lab-scale experiment is expensive and time-consuming, which needs further calibrations and validation before usage. Besides, the experiment is hard to capture detailed information at the particle scale level [8].

Numerical simulation is an alternative to study the fluidization process in fluidized beds with the increasing improvement of computer capacity [9,10]. Numerical simulation is capable to provide more detailed information of dense gas-solid flow than the experimental method without disturbing flow fields [11]. Multi-scale numerical methods have been proposed in the past decades [8,12], including the particle-resolved direct numerical simulation (PR-DNS), computational fluid dynamics-discrete element method (CFD-DEM), multi-phase particle-in-cell (MP-PIC), and two-fluid model (TFM), among which the CFD-DEM approach is the most suitable method for modelling dense gas-solid flow in lab-scale apparatuses with detailed particle trajectories and inter-particle collisions resolved at the particle-scale level [13]. With these advantages, the CFD-DEM approach is feasible for exploring the solid mixing and dispersion behaviours influenced by different operating parameters [14], such as particle properties [15], superficial gas velocity [11], bed width [16], and distributor type [17].

However, all the abovementioned work were focused on spherical particles without the real shape considered. In fact, particles in chemical engineering processes, such as biomass gasification, tablet coating, and food processing, have regular or irregular shapes [18]. Particle shape significantly affects the particulate behaviours in fluidized beds. For example, Shrestha et al. [19] demonstrated that ellipsoid particles had smaller bubble sizes and lower bubbling rising velocities than the spherical particles. Ren et al. [20] claimed that the spherical particles mixed more

* Corresponding author at: Midea Corporate Research Center, Foshan 528311, Guangdong, China.
E-mail address: zhangwt_12@163.com (W. Zhang).

https://doi.org/10.1016/j.powtec.2021.10.036
0032-5910/

evenly and faster than the corn-shaped particles. The mixing process varies for different particle shapes, attributed to the variations of cross-sectional area and the resulting gas-particle interaction force [21].

So far, only limited studies have been reported in the CFD-DEM simulation of the mixing and dispersion properties of non-spherical particles in fluidized beds. Vollmari et al. [22] numerically studied the mixing process of spherical particles and complex shaped particles in a BFB and demonstrated that the drag model should be modified by considering the particle shape and orientation. Abbaszadeh Molaei et al. [23] numerically investigated the mixing process of ellipsoid particles with a modified drag correlation proposed for multicomponent mixtures. They found that adding ellipsoid particles to the spherical particle bed reduced the minimum fluidization velocity. *Ma* et al. [24] numerically studied the fluidization of disk-like particles in a BFB and found that the disk-like with larger aspect ratios had stronger movement and more obvious fluidization. Mema et al. [25] numerically investigated the mixing characteristics of elongated cylindrical particles in a BFB and demonstrated that elongated particles presented more vigorous intermixing and shorter mixing time than the spherical particles. Although these studies shed light on the mixing process of irregular particles (e.g., disk-like, cylindrical) in fluidized beds, the mechanism of mixing and dispersion of ellipsoid particles is still far from being understood. Besides, the existing work mainly employed a multi-sphere model [25–27] or real geometry model to represent the non-spherical particles [28], however, a super-quadric model provides a better choice to describe the non-spherical morphology with numerical accuracy and computational cost balancing [29]. Via adjusting five typical parameters, more than 80% of particles in nature can be represented. Nowadays, the CFD-DEM approach coupled with the super-quadric model is popular to simulate the fluidization of non-spherical particles [19,30,31].

The novelty of the present work lies in two aspects: (i) development of a CFD-DEM approach coupled with the super-quadric model; (ii) underlying mechanism exploration of solid transportation intensity and mixing property of ellipsoid particles in fluidized beds. The drag model proposed by Hölzer and Sommerfeld [32] is employed to describe particle-gas interactions while the well-known Lacey mixing index is used to quantify the mixing degree of ellipsoid particles. The present work is organized as follows: Section 2 gives model details regarding the governing equations for the gas and solid phases, the drag model, and the numerical scheme. Section 3 gives the computational settings. The general flow patterns, solid mixing, and solid dispersion are presented in Section 4. Section 5 draws the conclusion.

2. Mathematical model

In this section, the CFD-DEM approach coupled with the super-quadric model is detailed, including the governing equations for the gas and solid phases, the collision model, and the drag model. The numerical scheme is finally presented.

2.1. Governing equations for the gas phase

Volume-averaged Navier-Stokes equations are employed to describe the gas phase with the voidage (ε_g) considered for the solid effect. The conservation equations of mass and momentum are given by:

$$\frac{\partial}{\partial t}\left(\varepsilon_g \rho_g\right) + \nabla\cdot\left(\varepsilon_g \rho_g \mathbf{u}_g\right) = 0 \tag{1}$$

$$\frac{\partial}{\partial t}\left(\varepsilon_g \rho_g \mathbf{u}_g\right) + \nabla\cdot\left(\varepsilon_g \rho_g \mathbf{u}_g \mathbf{u}_g\right) = -\varepsilon_g \nabla P_g + \varepsilon_g \rho_g \mathbf{g} + \varepsilon_g \nabla\cdot\boldsymbol{\tau}_g - \mathbf{F}_{pg} \tag{2}$$

where ρ_g is the gas density; $\mathbf{u}_g$ is the gas velocity vector; P_g is the gas pressure; μ_g is the gas viscosity. t is the time instant. $\mathbf{g}$ and $\mathbf{F}_{pg}$ are the gravity and inter-phase interaction force, respectively. The gas stress tensor $\boldsymbol{\tau}_g$ is written as:

$$\boldsymbol{\tau}_g = \mu_g \nabla \mathbf{u}_g + \mu_g \left(\nabla \mathbf{u}_g\right)^{\mathrm{T}} \tag{3}$$

where the gas turbulence is not considered. Specifically, the gas turbulence has been demonstrated to insignificantly influence coarse particles [33–35] and be commonly not resolved in many previous non-spherical particle simulations [19,30,36].

2.2. Governing equations for the solid phase

2.2.1. Representation and contact detection of ellipsoid particles

The accurate representation of non-spherical particles is significant for the calculation of contact forces, torques, and the resulting particle behaviours (e.g., trajectory, orientation, velocity). In this work, the non-spherical particle is represented by a super-quadric model [29]. The formulation for a non-spherical particle is given by:

$$f(x,y,z) = \left(\left|\frac{x}{a}\right|^{n_2} + \left|\frac{y}{b}\right|^{n_2}\right)^{n_1/n_2} + \left|\frac{z}{c}\right|^{n_1} - 1 = 0 \tag{4}$$

where five parameters, i.e., a, b, c, n_1, and n_2, control the particle shape. The first three parameters are semi-axis lengths along with the x, y, z directions, respectively. The last two parameters are the sharpness constants to adapt the curvature of particle edges. Over 80% of non-spherical particles encountered can be represented by the above super-quadric model by adjusting these five parameters [18,37]. For the ellipsoid particles studied in the present work, n_1 and n_2 are specified as 2 with adjusting a, b, and c to generate the following shapes as shown in Fig. 1. The aspect ratio (AR) is defined as the ratio of two semi-axis lengths. Thus, the super-quadric model balances model complexity and shape flexibility [29].

The present work employs a broad phase of the contact detection algorithm [29]. The non-spherical particle is encapsulated by a bounding sphere to significantly reduce the number of potential contact pairs. Due to the memory-efficient feature of the bounding sphere, the computational cost is significantly reduced. The deepest point method is used to calculate the maximum penetration/minimum distance between an interactive pair of particles.

2.2.2. Particle motion and forces

Newton's law of motion is employed to describe particle motions. The translational motion and rotational motion are expressed as:

$$m_i \frac{d\mathbf{v}_i}{dt} = m_i \mathbf{g} + \mathbf{f}_{c,i} + \mathbf{f}_{d,i} + \mathbf{f}_{p,i} \tag{5}$$

$$I_i \frac{d\boldsymbol{\omega}_i}{dt} + \boldsymbol{\omega}_i \times I_i \boldsymbol{\omega}_i = \boldsymbol{\tau}_i \tag{6}$$

where $\boldsymbol{\omega}_i$ and $\mathbf{v}_i$ are the rotational velocity and translational velocity of particle i, respectively. m_i and I_i are the mass and moment of inertia of particle i, respectively. $\mathbf{f}_{d,i}$ and $\mathbf{f}_{p,i}$ ($=-V_{p,i}\nabla P_g$) are drag force and pressure gradient force, respectively. $V_{p,i}$ is the particle volume. $\mathbf{f}_{c,i}$ is

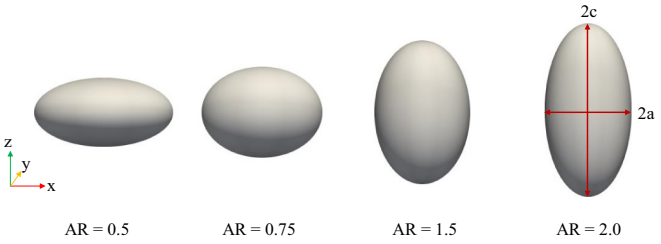

Fig. 1. Ellipsoid particles shaper with different aspect ratios (ARs), where the AR is defined as (2c/2a or 2c/2b), and $n_1 = n_2 = 2$.

the contact force, which can be calculated by the soft-sphere contact model originally proposed by Cundall and Strack [38] suitable for multiple collisions. In this work, only the gravity, collision force, drag force, and pressure gradient force are considered. Other forces, such as lift force (including Magnus and Saffman forces) and Basset force are neglected in simulating dense gas-solid flow with a large density ratio of particle to the gas phase ($\rho_p/\rho_g > 1000$) due to their insignificant contributions [39]. This strategy has been broadly employed in simulating ellipsoid particle fluidization [19,30]. Specifically, $\mathbf{f}_{c,i}$ can be divided into a normal component ($\mathbf{f}_{cn,ij}$) and a tangential component ($\mathbf{f}_{ct,ij}$) as follows:

$$\mathbf{f}_{cn,ij} = -k_{n,ij}\delta_{n,ij}\mathbf{n}_{ij} - \eta_{n,ij}\mathbf{v}_{n,ij} \tag{7}$$

$$\mathbf{f}_{ct,ij} = \begin{cases} -k_{t,ij}\delta_{t,ij}\mathbf{t}_{ij} - \eta_{t,ij}\mathbf{v}_{t,ij} & \text{for } |\mathbf{f}_{ct,ij}| \le \mu_s|\mathbf{f}_{cn,ij}| \\ -\mu_s|\mathbf{f}_{cn,ij}|\mathbf{t}_{ij} & \text{for } |\mathbf{f}_{ct,ij}| > \mu_s|\mathbf{f}_{cn,ij}| \end{cases} \tag{8}$$

where δ, k, and η are overlap displacement, spring coefficient, and damping coefficient, respectively. The subscripts n and t represent the variables in the normal direction and tangential direction, respectively. μ_s is the friction coefficient. $\mathbf{v}_{n,ij}$ and $\mathbf{v}_{t,ij}$ are the relative velocities. The spring and damping coefficients can be calculated according to particle properties [10].

It is easy to imagine that the normal contact can also induce torque due to the non-spherical morphology. Thus, the total torque exerting on particle i is written as:

$$\mathbf{T}_i = \mathbf{L}_i \times (\mathbf{f}_{cn,ij} + \mathbf{f}_{ct,ij}) \tag{9}$$

where $\mathbf{L}_i$ is the distance between the contact point and the particle centroid. For the non-spherical particle, a body-fixed coordinate system is introduced to calculate the orientation. The global coordinate system is used to evaluate the trajectory and velocity of each particle. The orientation of the non-spherical particle is represented by a quaternion of rotation $\mathbf{q}$ ($=[q_0, q_1, q_2, q_3]^T$). A transformation matrix $\mathbf{M}$ is employed to transfer the local and global variables as follows:

$$\mathbf{M} = \begin{pmatrix} 1-2(q_2^2+q_3^2) & 2(q_1q_2-q_0q_3) & 2(q_1q_3+q_0q_2) \\ 2(q_1q_2+q_0q_3) & 1-2(q_1^2+q_3^2) & 2(q_2q_3-q_0q_1) \\ 2(q_1q_3-q_0q_2) & 2(q_2q_3+q_0q_1) & 1-2(q_1^2+q_2^2) \end{pmatrix} \tag{10}$$

Thus, the transformation of torque and rotational velocity of particle i between the global system ($\mathbf{T}_i$, $\boldsymbol{\omega}_i$) and body-fixed system ($\boldsymbol{\tau}_i$, $\boldsymbol{\omega}_i'$) is given by:

$$\boldsymbol{\tau}_i = \mathbf{M}_i^{-1}\mathbf{T}_i \tag{11}$$

$$\boldsymbol{\omega}_i = \mathbf{M}_i\boldsymbol{\omega}_i' \tag{12}$$

2.3. Non-spherical drag model

The drag force acting on a non-spherical particle can be calculated by the following equation:

$$\mathbf{f}_{d,i} = \frac{1}{2}C_D\rho_g A_V|\mathbf{u}_g - \mathbf{v}_p|(\mathbf{u}_g - \mathbf{v}_p) = \frac{\beta_i V_{p,i}}{\varepsilon_g(1-\varepsilon_g)}(\mathbf{u}_g - \mathbf{v}_p) \tag{13}$$

where A_V is the cross-sectional area of the volume equivalent sphere. The drag coefficient C_D is calculated by combining the voidage and Reynolds number. The interphase momentum exchange coefficient β_i proposed by De Felice [40] has been widely to simulate dense gas-solid flow, which is given by:

$$\beta_i = \frac{3}{4}\frac{\varepsilon_g(1-\varepsilon_g)\rho_g|\mathbf{u}_g - \mathbf{v}_p|}{d_V}C_{D0}\varepsilon_g^{1-\chi} \tag{14}$$

$$\chi = 3.7 - 0.65\exp\left(-\frac{(1.5 - \log \mathrm{Re}_p)}{2}\right) \tag{15}$$

where C_{D0} is the drag coefficient for the individual non-spherical particle. Re_p is the particle Reynolds number. d_V is the diameter of a sphere with an equivalent volume of the non-spherical particle. The drag models proposed by Hölzer and Sommerfeld [32] and Ganser [41] are the most used ones in simulating the fluidization of non-spherical particles. Gao et al. [36] demonstrated that the former provided a better prediction of bed hydrodynamics than the latter. Thus, the drag model proposed by Hölzer and Sommerfeld [32] is employed in the present work. It considers the particle orientation and particle shape as:

$$C_{D0} = \frac{8}{\mathrm{Re}_p}\frac{1}{\sqrt{\varphi_\perp}} + \frac{16}{\mathrm{Re}_p}\frac{1}{\sqrt{\varphi}} + \frac{3}{\sqrt{\mathrm{Re}_p}}\frac{1}{\varphi^{3/4}} + 0.42 \times 10^{0.4(-\log(\varphi))^{0.2}}\frac{1}{\varphi_\perp} \tag{16}$$

where the regular sphericity φ is a ratio between the surface area of the volume equivalent sphere and that of the real particle. $\varphi_\perp = d_V^2/d_\perp^2$ is the crosswise sphericity, a ratio between the cross-sectional area of a volume equivalent sphere and the projected cross-section area of the non-spherical particle normal to the flow. The projected area of a non-spherical particle is calculated in the body-fixed coordinate system. For the ellipsoid particle, the projected area $A_\perp$ is given by [36]:

$$A_\perp = \pi\left(l^2b^2c^2 + m^2c^2a^2 + n^2a^2b^2\right)^{1/2} \tag{17}$$

2.4. Interpolation method

In the CFD-DEM approach, the Lagrangian quantities of particles (e.g., volume $V_{p,i}$, force $\mathbf{f}_{d,i}$) are interpolated into the Eulerian grids to calculate the voidage (ε_g) and inter-phase interaction forces ($\mathbf{F}_{pg}$). The two commonly used methods are the particle centroid method (PCM) and the divided particle volume method (DPVM). However, considering numerical stability and numerical accuracy, the former method which needs the grid size to be more than 3.82 times the particle diameter is not selected [42]. In this work, the DPVM is used to calculate the voidage and interphase interaction force as follows:

$$\varepsilon_{g,j} = 1 - \sum_{i=1}^{N_p}\frac{w_{i,j}V_{p,i}}{V_{cell,j}} \tag{18}$$

$$\mathbf{F}_{gp,j} = \sum_{i=1}^{N_p}\frac{w_{i,j}\mathbf{f}_{d,i}}{V_{cell,j}} \tag{19}$$

where $V_{cell,j}$ and $w_{i,j}$ are the cell volume and spatial weight, respectively. N_p is the particle number. Specifically, the super-quadric particle is uniformly divided into N ($=N_x \times N_y \times N_z$) sub-boxes. The spatial weight can be obtained by summing all sub-boxes in the current cell as follows:

$$w_{i,j} = \frac{N_{i,j}}{N_{in}} \tag{20}$$

2.5. Numerical scheme

The governing equations for the gas phase are discretized by the finite volume method (FVM) [43]. The transient time term is integrated by a second-order Crank-Nicolson scheme. The convection and diffusion terms are discretized by a second-order central differencing scheme. The coupling between the gas pressure and velocity is treated by a Pressure-Implicit Split-Operators (PISO) scheme [44]. The particle information (e.g., position, velocity) is obtained by explicitly integrating the

governing equations for the solid phase. Fig. 2 shows the coupling procedure between the CFD and DEM solvers. Via the initial particle information, the voidage and inter-phase interaction forces are calculated. Then, the pressure and velocity of the gas phase are obtained by solving the volume-averaged Navier-Stokes equations. After then, the particle information (e.g., velocity, position) is calculated by the DEM solver by considering the gravity, contact force, drag force, and pressure gradient force. The updated particle information is fed back to the CFD solver to complete the next calculation loop.

As shown in Fig. 2, the CFD solver and DEM solver are controlled by the corresponding time steps. For the CFD solver, the time-step of the gas phase is monitored by the Courant–Friedrichs–Lewy (CFL) number [43]:

$$\mathrm{CFL} = \Delta t_g \max\left(\frac{|\mathbf{u}_f|}{\Delta x}\right) < 1 \tag{21}$$

where Δx is the grid size. The gas time-step (Δt_g) is several times of the solid time step (Δt_p). For the DEM solver, the Rayleigh time (Δt_{Ray}) is introduced to determine the solid time step [45,46]:

$$\Delta t_p = \alpha \Delta t_{Ray} = \frac{\alpha \pi d_p}{2(0.1631\upsilon_p + 0.8766)} \sqrt{\frac{2\rho_p(1+\upsilon_p)}{Y_p}} \tag{22}$$

where ρ_p, Y_p, and υ_p are the particle density, particle Young's modulus, and particle Poisson ratio, respectively. α is a constant, ranging from 0.1 to 0.5 to ensure numerical stability [47–49].

2.6. Model validation

In this section, the super-quadric model is first validated towards the discharge process of ellipsoid particles in a hopper, and the CFD-DEM approach is then validated towards the gas-solid flow dynamics in a BFB.

The first validation is towards the discharge process of ellipsoid particles in a flat bottom hopper experimentally carried out by Liu et al. [50]. The investigated object is a rectangular column with the dimension of 290 mm, 55 mm, and 1000 mm in *x*, *y*, and *z* directions, respectively. An orifice with a dimension of 55 mm × 54 mm is located in the centre bottom of the hopper. The ellipsoid particles are described by the following properties: 2a = 2b = 13.56 mm, 2c = 7.19 mm. A total number of 5500 ellipsoid particles with a density of 1338 kg/m^3 are packed in the hopper with an initial bed height of about 0.43 m. Details about the gas-solid properties are listed in Table 1.

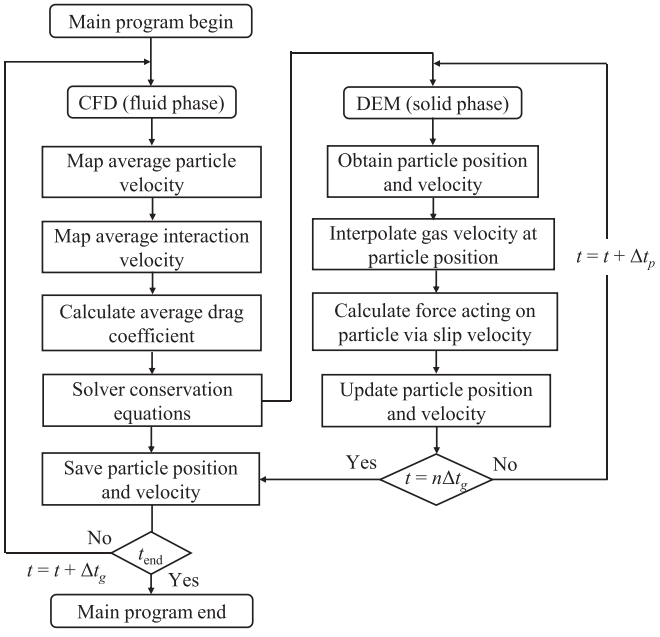

Fig. 2. Flow chart of the coupling procedure of CFD-DEM simulation of non-spherical particles.

Table 1
Gas-solid parameters in the first model validation.

Parameter	Value	Unit
Axis, 2a = 2b	13.56	mm
Axis, 2c	7.19	mm
Particle density (ρ_p)	1338	kg/m^3
Young's modulus (Y_p)	1×10^7	Pa
Poisson ratio (ν_p)	0.29	–
Restitution coefficient (e_p)	0.5	–
Friction coefficient (μ_p)	0.5	–

Fig. 3 gives the comparison of the predicted discharge process and experimental observation [50] at different time instants. In general, a V-shape particle flow pattern driven by gravity is well predicted by the super-quadric model. The predicted discharge rate is also quantitatively compared with the experimental data as shown in Fig. 4. The good agreement demonstrates the reliability of the super-quadric model in predicting the behaviours of ellipsoid particles.

The second model validation refers to the gas-solid flow in a BFB experimentally conducted by Müller et al. [51]. The geometry configuration is a rectangular column with a dimension of 0.044 m, 0.2, and 0.01 in width, height, and depth, respectively. The computational domain is divided into 15, 68, and 3 in three directions, respectively. The particles with a diameter of 1.2 mm and a density of 1000 kg/m^3 are randomly packed in the lower part of the bed. The total number of particles is 9240. The airflow is introduced from the bottom distributor with a superficial gas velocity of 0.6 and 0.9 m/s, i.e., 2.0 times minimum fluidization velocity (U_{mf}) and 3.0 U_{mf}, respectively. The detailed gas-solid parameters are listed in Table 2. As shown in Fig. 5, the time-averaged solid velocity and voidage show maximum values in the central region and decrease along with the horizontal direction, indicating that the bubbles with high velocities concentrate in the central region. The downward particle flow is also successfully captured. Some slight discrepancies between the simulation and experimental data appear in the central region and close to the wall, which may be attributed to the over-prediction of bubble size. However, the present study gives a better numerical prediction than the Ref. [51]. In general, the predicted solid velocity and voidage agree well with the experimental data, demonstrating the reasonability of the CFD-DEM approach in reproducing gas-solid flow in fluidized beds.

3. Simulation conditions

The investigated object is a fluidized bed with 0.252 m, 1.008 m, and 0.024 m in width, height, and depth, respectively. As shown in Fig. 6a, ellipsoid particles with an aspect ratio (AR) ranging from 0.75 to 2.0 are packed in the lower part of the bed. In this work, the equivalent diameter (d_V) fined as the diameter of a spherical particle with the same volume as an ellipsoid particle is set to 4.0 mm. All ellipsoid particles with different ARs have the same volume. The particle density is 1450 kg/m^3 and the particle number is 35000. Details of the gas-solid particles are listed in Table 3. As shown in Fig. 6b, the grid number in along with three directions is 21, 2, and 84, respectively. Thus, the average grid size is 12 mm, 2– 3 times the particle diameter, which meets the DPVM requirement that the grid size should be larger than the particle size [42]. Before the simulation, the boundary condition should be properly set. For the velocity, the bottom is set as uniform velocity, the top is set as zero gradients, and the wall is set as no-slip velocity; for the pressure, the top is set as atmospheric temperature and other walls are set as zero gradients. The front and back walls are specified

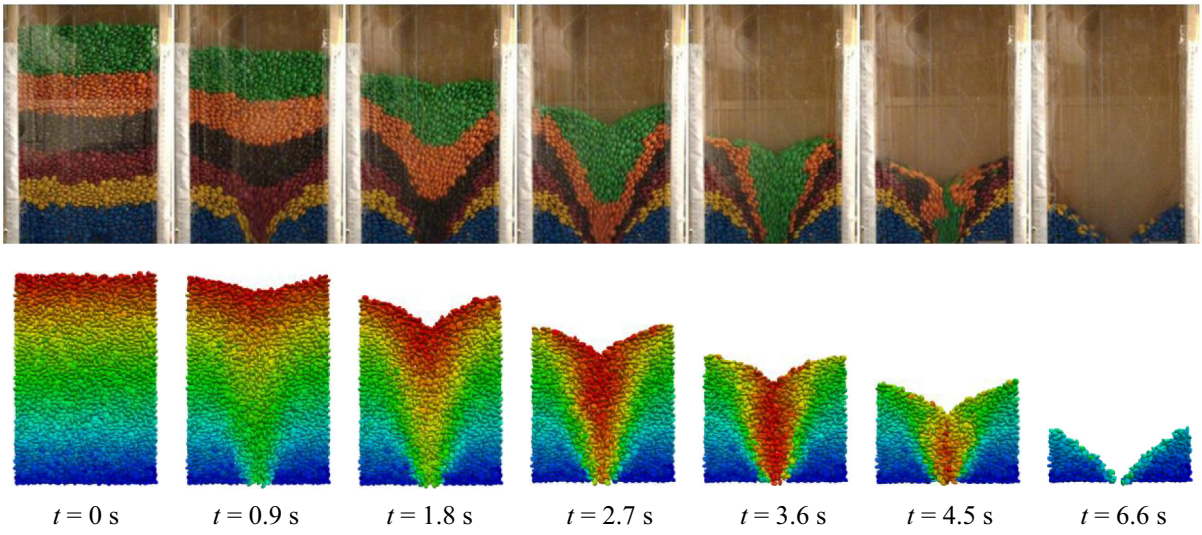

Fig. 3. Snapshots of chocolate candies discharging from a hopper at different times: (top) experiment of Liu et al. [50], (bottom) super quadric DEM simulation.

as periodic boundary conditions to eliminate the wall effect on particles behaviours.

Initially, ellipsoid particles are generated from a surface at the height of 0.6 mm and then fall under the effect of gravity. After the kinetic and rotational energies of ellipsoid particles are dissipated to zero, the airflow is introduced from the bottom distributor. The minimum fluidization velocity (U_{mf}) for each type of ellipsoid particle is predicted in the next section. The time-step for the gas phase is 1×10^{-5} s while that for the solid phase is 1×10^{-6} s.

4. Results and discussion

4.1. General flow patterns

The U_{mf} is determined by the method proposed by Rhodes et al. [14]. The superficial gas velocity (U_g) increases step by step over time and the pressure drop is monitored by two points, i.e., one point is located above the bottom distributor and another point is located above the bed surface. As shown in Fig. 7, the pressure drop increases with the augment of superficial gas velocity. When the superficial gas velocity reaches a certain value, the pressure drop sharply decreases and fluctuates around a fixed value. The superficial gas velocity corresponding to the alternation point is defined as minimum fluidization velocity. The decrease of the pressure drop is attributed to the breaking of the interlocking state of the initial bed material. Ellipsoid particles with different aspect ratios lead to different bed porosities. Thus, it demonstrates that the bed permeability is dependent on the bed porosity and particle shape. It is interesting to note that the minimum fluidization velocity increases with the AR, which is consistent with the Ergun prediction modified for non-spherical particles [52]. The minimum fluidization velocity of ellipsoid particles at AR = 0.5, 0.75, 1.5, and 2.0 are 0.6 m/s, 0.825 m/s, 0.95 m/s, and 0.975 m/s, respectively.

Fig. 8 illustrates the general flow patterns regarding the voidage and particle velocities over time in the bed. Initially, after the airflow is vertically introduced from the bottom distributor, the bed expansion can be observed at $t = 0.05$ s. The original interlocking status is broken with the formation of regions of ellipsoid particles with upward velocities and significant velocity gradients. Owing to drastic gas-particle momentum exchanges induced by vigorous airflow, the ellipsoid particles are raised to the upper part of the bed. Under the combined effects of gravity, inert-particle collisions, energy dissipation, and wall restriction, the particles reaching the maximum height fall along the two side walls ($t = 0.5$ s). The downward particles collide with the upward particles, forcing particles into instantaneous trajectories. Bubbles place a significant role in determining the flow patterns at different time instants.

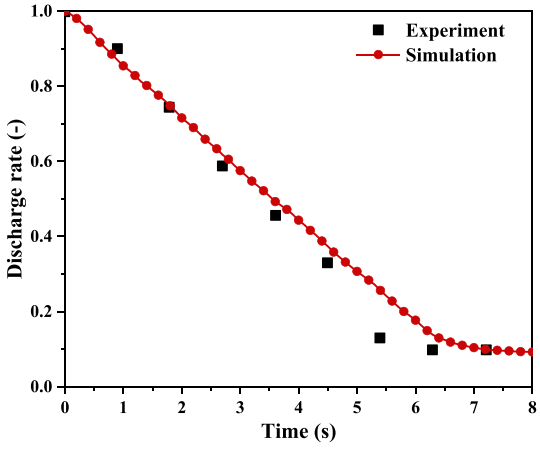

Fig. 4. Comparison of the predicted ratio of the particles remaining in the hopper over time and experimental data [50].

Table 2
Geometry and gas-solid parameters in the second model validation.

Parameter	Value	Unit
Bed width (W)	0.044	m
Bed height (H)	0.2	m
Bed depth (D)	0.01	m
Grid number ($N_W \times N_H \times N_D$)	$15 \times 68 \times 3$	–
Solid property		
Particle number (N_p)	9240	–
Particle density (ρ_p)	1000	kg/m^3
Particle diameter (d_p)	1.2	mm
Young's modulus (Y_p)	0.12	MPa
Poisson ratio (ν_p)	0.33	–
Restitution coefficient (e_p)	0.97	–
Friction coefficient (μ_p)	0.1	–
Gas property		
Gas density (ρ_g)	1.225	kg/m^3
Gas viscosity (μ_g)	1.8×10^{-5}	kg/(m·s)
Superficial gas velocity (U_g)	0.6, 0.9	m/s

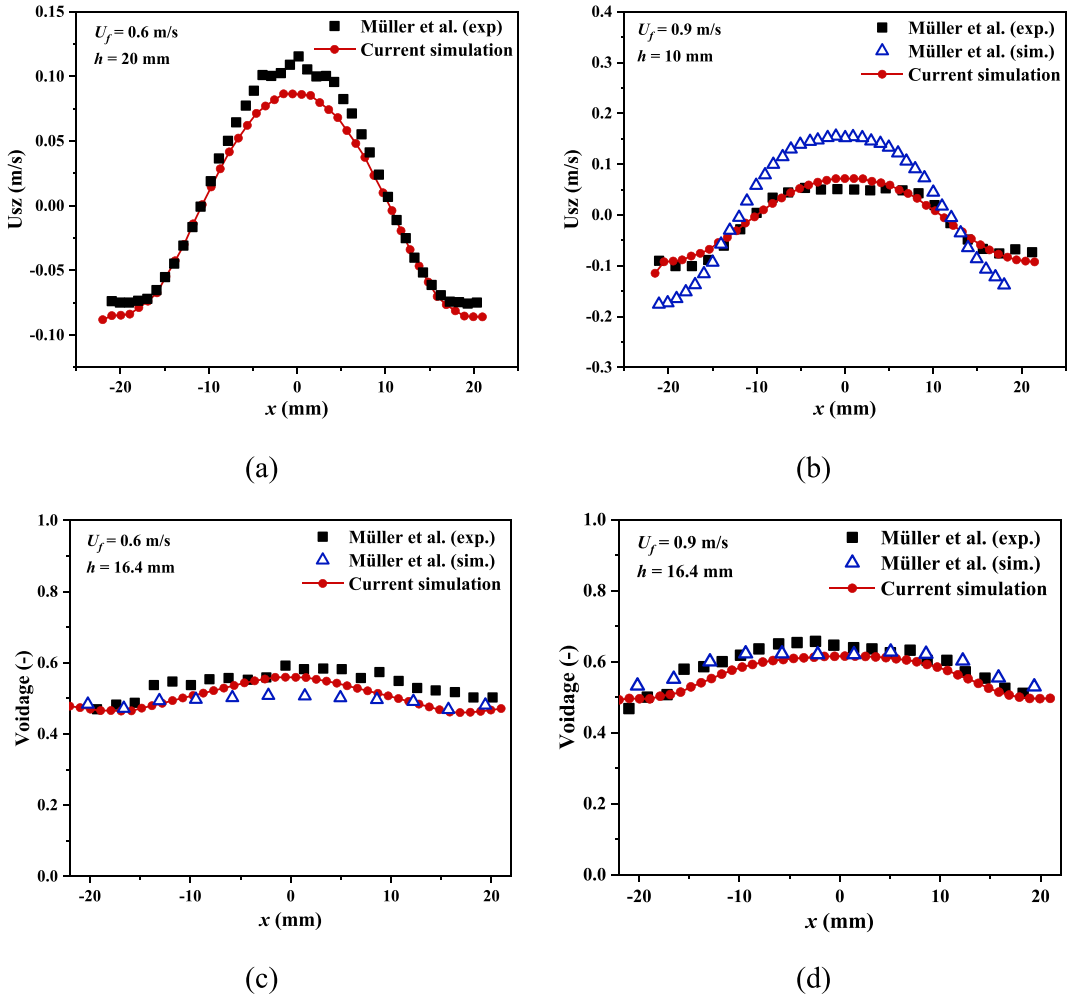

Fig. 5. Comparison of time-averaged solid vertical velocity (Usz) and voidage between experiment [51] and current simulation at different bed heights: (a) $U_f = 0.6$ m/s, $h = 20$ mm; (b) $U_f = 0.9$ m/s, $h = 10$ mm; (c) $U_f = 0.6$ m/s, $h = 16.4$ mm; (d) $U_f = 0.9$ m/s, $h = 16.4$ mm.

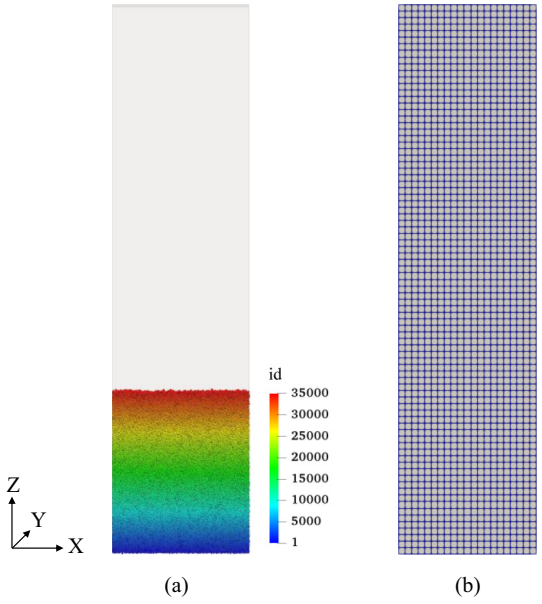

Fig. 6. Geometry (left) and grids (right) of the investigated fluidized bed.

Table 3
Geometry and gas-solid parameters in the simulation.

Parameter	Value	Unit
Bed width (W)	0.252	m
Bed height (H)	1.008	m
Bed depth (D)	0.024	m
Grid number ($W \times H \times D$)	21 × 2 × 84	–
Particle property		
Oblate, AR (a × b × c)	0.5 (2.52 × 2.52 × 1.26) 0.75 (2.2 × 2.2 × 1.66)	mm
Prolate, AR (a × b × c)	1.5 (1.74 × 1.74 × 2.62) 2.0 (1.58 × 1.58 × 3.16)	mm
Particle number (N_p)	35,000	–
Particle volume equivalent diameter, (d_V)	4.0	mm
Particle density (ρ_p)	1450	kg/m^3
Young's modulus (Y_p)	1.0×10^7	Pa
Poisson ratio (ν_p)	0.3	–
Restitution coefficient (e_p)	0.6	–
Friction coefficient (μ_p)	0.4	–
Gas property		
Gas density (ρ_g)	1.205	kg/m^3
Gas viscosity (μ_g)	1.8×10^5	kg/(m·s)
Superficial gas velocity (U_g)	2.0 U_{mf}	m/s

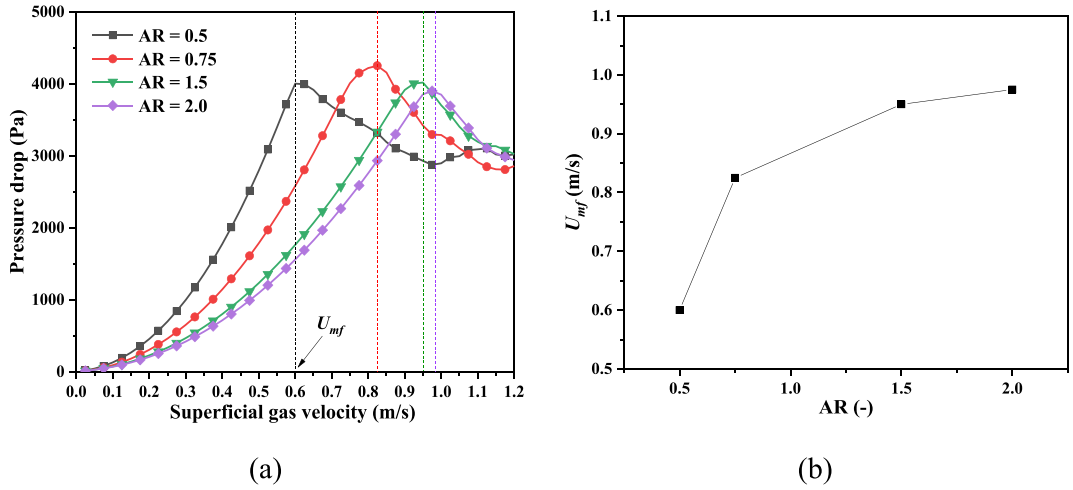

Fig. 7. The prediction of minimum fluidization velocity (U_{mf}) at different aspect ratios (ARs): (a) pressure drop against the superficial gas velocity; (b) U_{mf} at different ARs.

Small bubbles are randomly generated from the bottom distributor and merge with the surrounding bubbles during the rising procedure. Particles are entrained by the bubble wake and move upwards in the central region of the bed. The eruption of bubbles at the bed surface throws particles into the freeboard. Some "bridges" around the bubble and close to the wall are observed, which is also evidenced in the previous simulation towards rod-like particles [52]. Due to the aspect ratio, non-spherical particles are easier to be hindered by the surrounding particles than spherical particles. At $t = 2.0$ s, 3.0 s, and 10 s, a particle jet with high vertical velocities appears in the preferential path of the rising bubbles.

Time-averaged flow patterns are given in Fig. 9. The typical core-annulus flow structure is captured, in which the dilute phase in the central region has a positive velocity due to the vigorous bubble evolution while the dense phase close to the wall presents a negative velocity due to the gravity and wall effects. The central region along with the bed height is the preferential path of bubbles, which is formed due to the wall restriction. With the increase of bed width, the preferential path will be mitigated, and bubbles are distributed uniformly in the bed [19]. As shown in Fig. 9b, two blue regions close to the side walls represent the back-mixing of falling particles. Due to the bubble evolution, the well-known solid circulation appears, where particles are lifted through the centre, move horizontally above the bed surface (Fig. 9c), and finally move downwards along the walls. It is noted that a double-recirculation pattern in which particles mainly moves from the wall to the centre in the lower bed and oppositely in the upper bed is formed. It demonstrates that the non-sphericity delays the fluidization of ellipsoid particles, at high superficial gas velocities, the solid circulation is qualitatively similar to that of the spherical particles. The spatial distribution of solid velocities of the ellipsoid particles in the present study is comparable to that of the rodlike particles reported in the literature [7,26].

The voidage distributions at the bed height of 0.2 m and 0.4 m under different aspect ratios are quantitatively compared in Fig. 10. In general, maximum voidage appears in the central region with the decreased trend observed along with the horizontal direction. At the lower part of the bed (i.e., H = 0.2 m), particles with the larger sphericities (e.g., AR = 0.75, 1.5) give a higher voidage in the central region, which demonstrates the bubble evolution is more vigorous in these two scenarios. The solid back-mixing is intensified close to the wall region. Aspect ratio performs a slight influence on the voidage distribution at the medium part of the bed (i.e., H = 0.4 m) due to the dilute phase in the central region near the bed surface.

Fig. 11 gives the influence of aspect ratio on the vertical velocity distribution at different bed heights. The ellipsoid particle will approach a sphere when the AR closes to 1. Thus, ellipsoid particles with AR = 0.75 and 1.5 have high sphericity. As shown in Fig. 11, ellipsoid particles with higher sphericity (AR = 0.75, 1.5) show a larger Usz in the bed than that with lower sphericity (AR = 0.5, 2.0). This phenomenon has also been evidenced in the simulation regarding non-spherical particle fluidization in a spouted bed [28]. Reasons lie in that the non-spherical particles with lower sphericity (i.e., AR = 0.5, 2.0) form more "bridges" around the bubbles, which hinder the bed permeability and particle motions [52]. This demonstrates that a higher superficial gas velocity is needed for the good fluidization of ellipsoid particles with lower sphericity (i.e., smaller or larger AR). Positive solid vertical velocity in the central region means the upward motion of particles while negative solid vertical velocity close to the wall indicates the particle back-mixing phenomenon. The upward motion in the centre and downward motion near walls drives the solid circulation in the whole bed. The velocity distributions at different heights predicted in the present work show agreement with that in the previous literature [7,26], demonstrating the reasonability of the present model in simulating ellipsoid particles.

Fig. 12 shows the effects of aspect ratio on horizontal velocity distribution at different heights. The distribution is symmetrical at the higher height (i.e., H = 0.4 m), because the gas-solid flow is chaotic in the lower part of the bed attributed to the combined effects of intense particle-particle/gas interactions, bubble-emulsion phase interactions, and gas entrance. The horizontal velocity is smaller in the lower region (i.e., H = 0.2 m) than that in the upper region (i.e., H = 0.4 m) due to the dominant role of vertically introduced airflow.

4.2. Solid mixing

Solid mixing is a significant property of dense particulate flow in chemical engineering reactors, which directly affects the heat and mass transfer and the resulting reactor performance. In a fluidized bed, the fully mixed and fully segregated patterns are two extreme states for a particle mixing process. The mixing characteristics can be identified by various mixing indices. In the present study, the well-known Lacey index (MI) is employed to assess the mixing degree of non-spherical particles in the fluidized bed. MI is defined as [53]:

$$\mathrm{MI} = \frac{\sigma_0^2 - S^2}{\sigma_0^2 - \sigma_r^2} \tag{23}$$

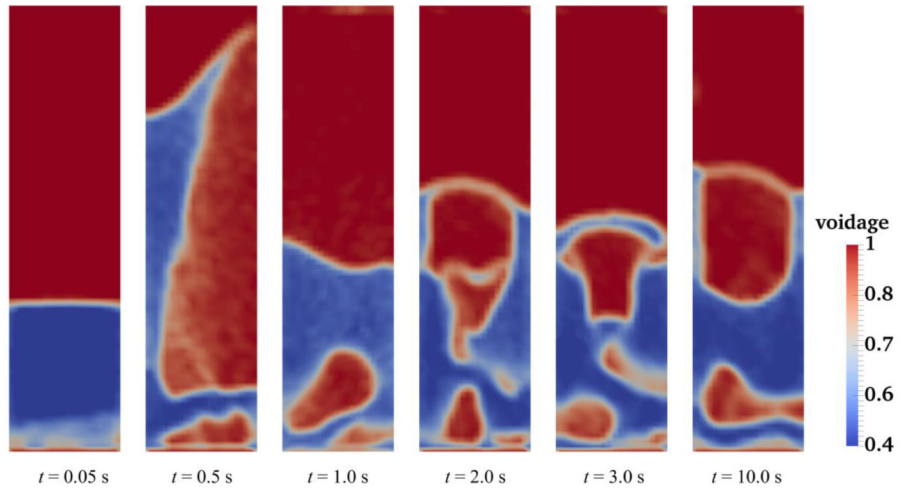

(a)

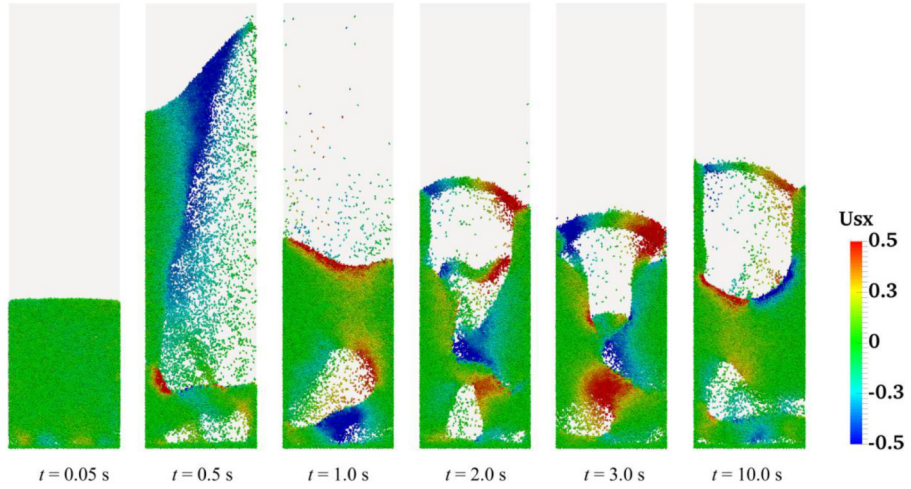

(b)

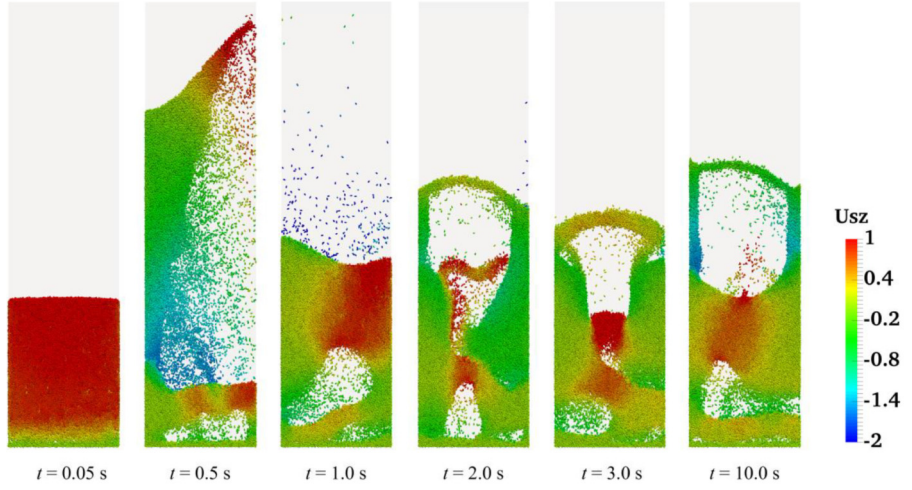

(c)

Fig. 8. Snapshots of ellipsoid particles in the BFB at $U_f/U_{mf} = 2.0$ and AR = 2.0: (a) voidage; (b) solid horizontal velocity (Usx); (c) solid vertical velocity (Usy).

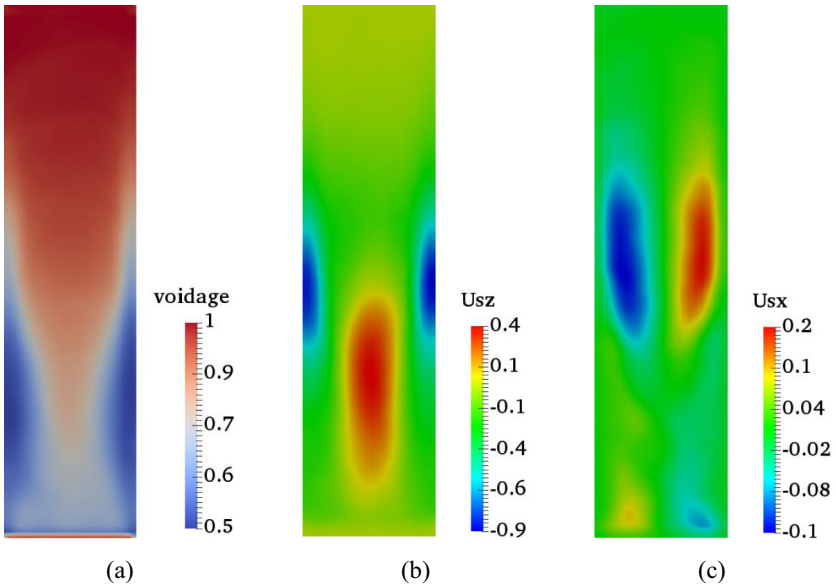

Fig. 9. Time-averaged quantities in the central slice (Y = 0 mm): (a) voidage; (b) solid vertical velocity (Usz); (c) solid horizontal velocity (Usx).

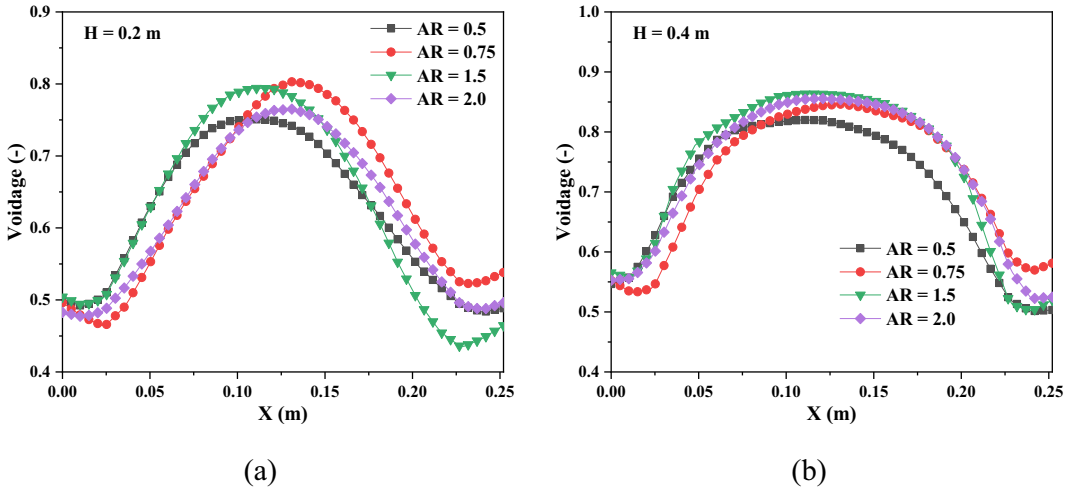

Fig. 10. Time-averaged voidage in the horizontal direction at different heights: (a) H = 0.2 m; (b) H = 0.4 m.

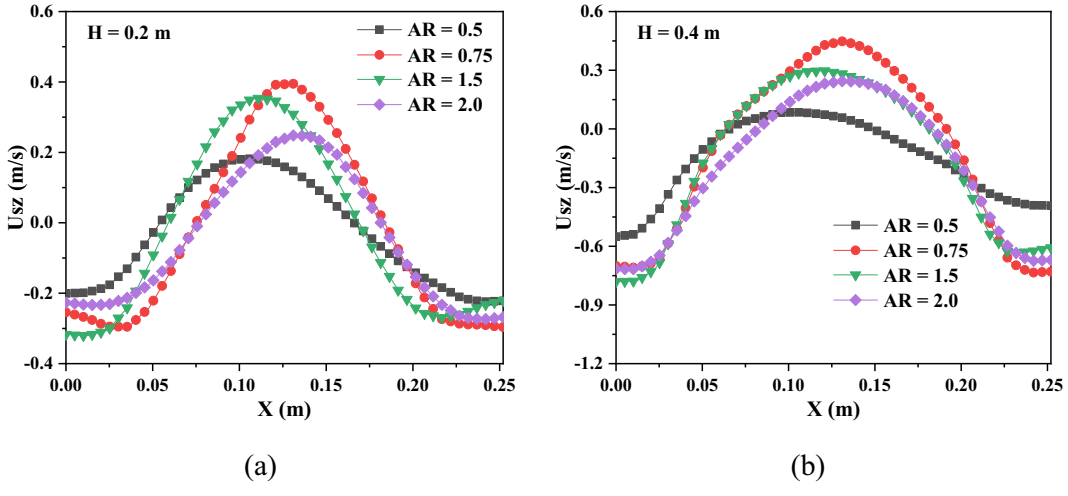

Fig. 11. Time-averaged solid vertical velocity in the horizontal direction at different heights: (a) H = 0.2 m; (b) H = 0.4 m.

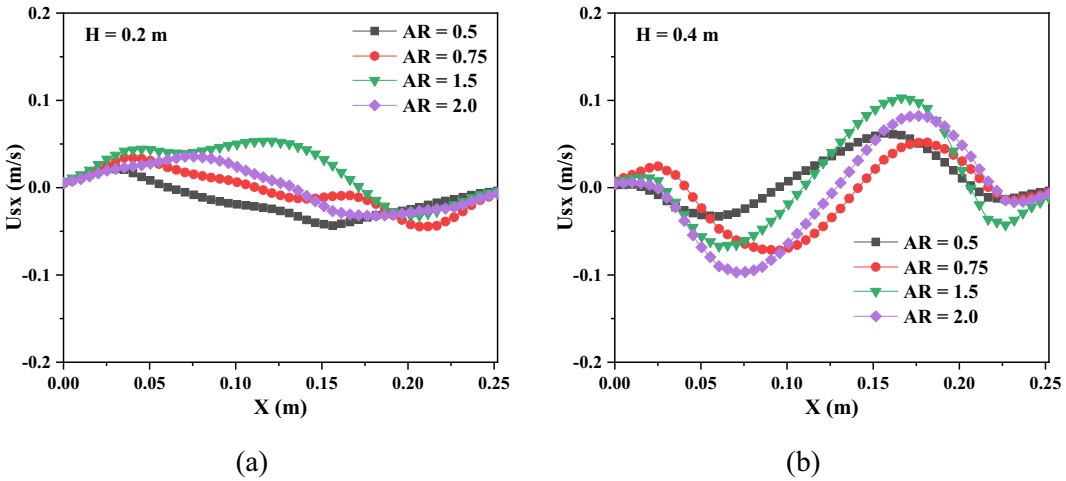

Fig. 12. Time-averaged solid horizontal velocity in the horizontal direction at different heights: (a) H = 0.2 m; (b) H = 0.4 m.

$$\sigma_0^2 = \bar{c}(1-\bar{c}), \sigma_r^2 = \bar{c}(1-\bar{c})/\bar{n}, S^2 = \frac{1}{N-1}\sum_{i=1}^{N}(\bar{c}-c_i)^2 \quad (24)$$

where σ_0^2 stands for the fully segregated state and σ_r^2 denotes the completely mixed state. $\bar{c}$ means the mean concentration of a specific component. $\bar{n}$ is the mean number of a specific component. In contrast, c_i and n are the concentration of a specific component. S^2 is the variance of solid mixing. N represents the total number of sampling cells. Thus, MI = 1 indicates a fully mixed state while MI = 0 corresponds to a completely segregated state. The solid mixing index of the particulate system at any time instant is in the range of 0 and 1.

Before quantifying the mixing state, the influence of sampling cell size on the mixing index should be evaluated. As shown in Fig. 13a, particles in the bed are labelled by two colours (i.e., yellow and blue) and the sampling cell is a volume containing several particles with different colours. In this work, three sets of sampling cell size are assigned, i.e., 0.0168 × 0.02 × 0.0168 mm^3, 0.02 × 0.02 × 0.02 mm^3, 0.0223 × 0.02 × 0.0223 mm^3. As shown in Fig. 13b, the mixing index is insensitive to the sampling cell size. It is because sufficient particles are selected for these three sets of sampling cells. Moreover, the post-processing of data using these three sets of sampling cells requires a similar computational demand. Thus, the medium sampling cell is used for the following analysis of the mixing process.

The mixing process of ellipsoid particles with AR of 2.0 in the BFB is illustrated in Fig. 14. At the beginning with the introduction of vertical airflow, an intense bed expansion is observed, which is almost two times the static bed height. As time marches, yellow particles migrate and mix with the blue particles in the medium part of the dense bed.

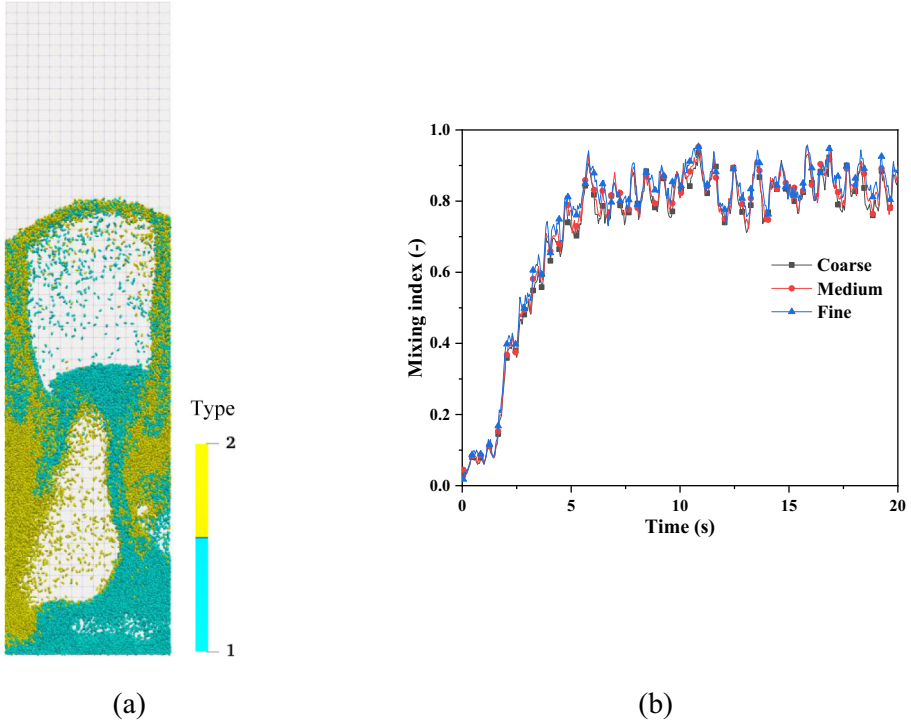

Fig. 13. Illustration of sampling method, U_f/U_{mf} = 2.0 and AR = 2.0: (a) mixing pattern at t = 2.5 s; (b) mixing index with different sampling sizes, i.e., 0.0168 × 0.02 × 0.0168 mm^3 (fine), 0.02 × 0.02 × 0.02 mm^3 (medium), 0.0223 × 0.02 × 0.0223 mm^3 (coarse).

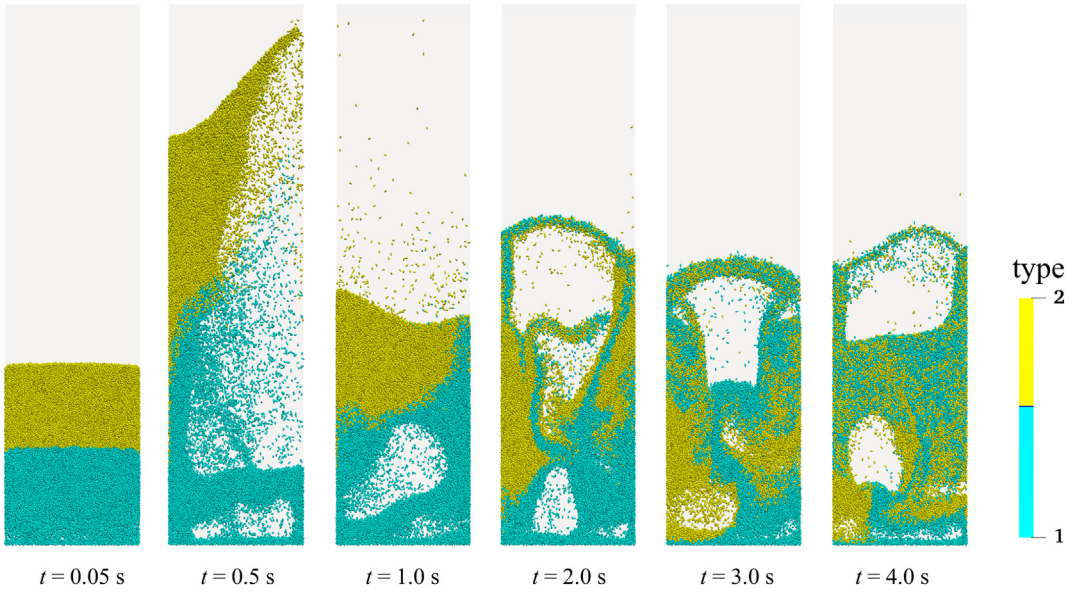

Fig. 14. Snapshots of ellipsoid particles mixing in the BFB at $U_f/U_{mf} = 2.0$ and AR = 2.0.

Bubble dynamics (e.g., generation, rising, coalescence, and eruption) drives the mixing process both in horizontal and vertical directions. At $t = 4.0$ s, a large proportion of yellow particles are transported into the lower part of the dense bed, and two types of particles fully mix in the upper part of the dense bed. As this process progresses, solid mixing in the system will finally approach the equilibrium state. Thus, we can divide the mixing process into three stages: the unsteady start-up state (~0.5 s), the vigorous mixing state (~4.0 s), and the final steady state. The second stage driven by bubble dynamics dominates the whole mixing process in the bed.

The mechanism of the mixing process is further discussed. The mixing can be categorized into three types, convective mixing, shear mixing, and diffusive mixing [54]. The convective mixing is significant when the particles are lifted from the bottom region to the upper region by airflow. Upward particles with positive vertical velocities, downward particles with negative vertical velocities, and the particles with horizontal velocities interconnect in the bed. The shear mixing takes place along the interface of two particulate flows. Shear mixing also affects the vigorous mixing stage. Particles at the bed surface are scattered into the freeboard, in which the diffusive mixing plays a significant role. It is noted that particles in the upper region of the bed are well better mixed than those in the lower region. In summary, the convective mixing and shear mixing is significant to establish the "coarse mixing stage", while the diffusive mixing accomplishes the "fine mixing stage" to make the system approach the equilibrium state [54].

Fig. 15 gives the influence of aspect ratio on the mixing index in the BFB. In general, the mixing indices with different aspect ratios rapidly increase and then fluctuates around the fixed value after 10 s, indicating the system reaches an equilibrium state. The average mixing index during the equilibrium state as shown in Fig. 15b indicates that ellipsoid particles with higher sphericity (e.g., AR = 0.75 and 1.5) show a smaller mixing index in the bed. The relationship between AR and averaging mixing index can be fitted with a polynomial function.

4.3. Solid dispersion

Solid dispersion is an important indicator to evaluate the solid transportation intensity in chemical engineering reactors, determining the solid residence time and the conversion degree. As reported in the literature [16,55,56], the solid dispersion coefficient in fluidized beds is in

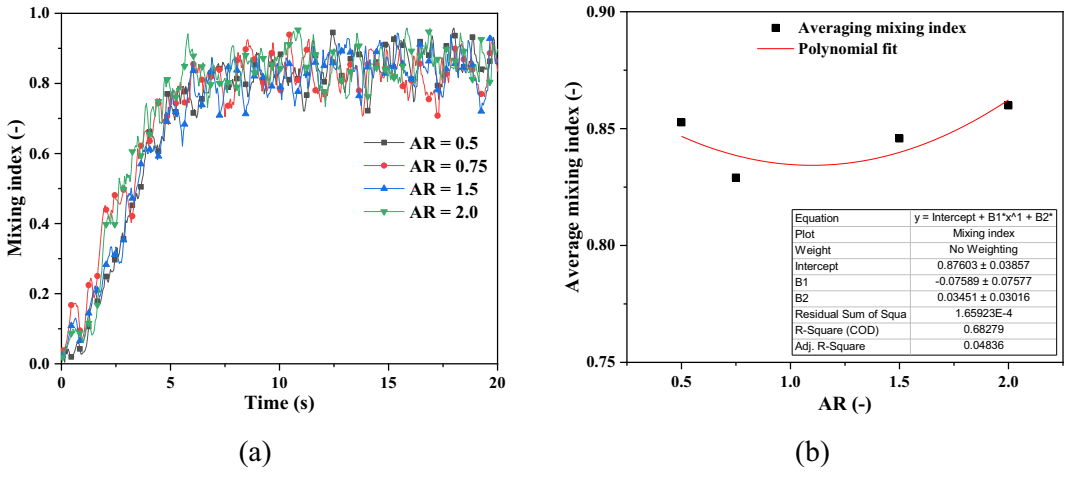

Fig. 15. Time-evolution (a) and average (b) mixing indices at different ARs.

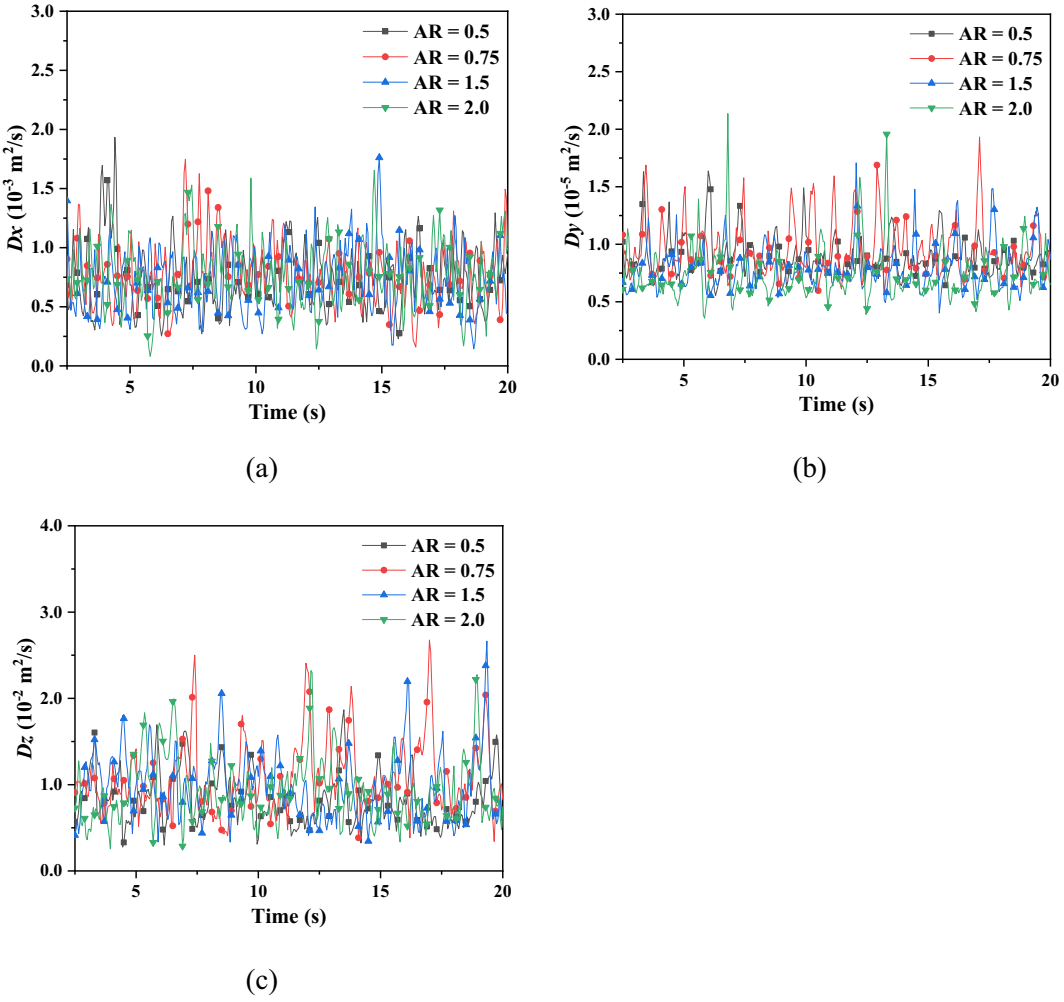

Fig. 16. Time-evolution profiles of dispersion coefficients in three directions at different ARs: (a) dispersion coefficient in *x* direction (*Dx*); (a) dispersion coefficient in *y* direction (*Dy*); (a) dispersion coefficient in *z* direction (*Dz*).

the range of 10^{-4} m^2/s and 10^{-1} m^2/s. The solid dispersion coefficient (D_i) for particle *i* is formulated as [16]:

$$D_i = \frac{(\Delta r_i)^2}{2\Delta t} \tag{25}$$

where Δr_i represents particle displacement in the time interval Δt, which is highly dependent on the particle-particle collisions and particle-gas interactions at the micro-scale level. The particle displacement can be calculated between the position at the present time instant and the previous time instant. The average solid dispersion coefficient (D) is used to assess the transportation intensity of all particles (N_p) in the system:

$$D = \frac{1}{N_P}\sum_{i=1}^{N_P}\frac{(r_i - r_{i0})^2}{2\Delta t} \quad (i = 1, 2, \ldots, N_P) \tag{26}$$

The solid dispersion coefficients in three directions (i.e., *Dx*, *Dy*, *Dz*) at different aspect ratios are shown in Fig. 16. In general, the solid dispersion coefficients fluctuate around the fixed values. The magnitude of the *Dx*, *Dy*, and *Dz* is about ~10^{-3} m^2/s, ~10^{-5} m^2/s, and ~ 10^{-2} m^2/s, respectively. For a quasi-2D simulation, the particle motion is limited by the front and rear walls, and thus the solid transportation intensity along with the bed depth is the smallest. The vertical introduction of the airflow leads to vigorous motion along with the bed height; thus, the solid axial transportation intensity is the largest. It is noted that the solid dispersion coefficients for the ellipsoid particles are all consistent with the magnitude evidenced in the literature [16,55,56].

Table 4 gives the time-averaged solid dispersion coefficients at different aspect ratios. It is interesting to find that the ellipsoid particles with higher sphericity (e.g., AR = 0.75 and 1.5) show larger solid dispersion intensity. The solid dispersion coefficient along with axal direction is one order of magnitude larger than that along with the horizontal direction.

Table 4
Time-averaged solid dispersion coefficients at different ARs.

	AR = 0.5	AR = 0.75	AR = 1.5	AR = 2.0
Dx (10^{-3} m^2/s)	0.7142	0.7794	0. 7577	0.7406
Dy (10^{-5} m^2/s)	0.8858	0.9496	0.7954	0.7469
Dz (10^{-2} m^2/s)	0.8260	1.1085	0.9761	0.9673

5. Conclusion

In this work, the CFD-DEM approach is extended to explore the mixing and dispersion characteristics of ellipsoid particles in a bubbling fluidized bed (BFB). The morphology of the ellipsoid particle is described by a super-quadric model and inter-particle collisions are resolved by a soft-sphere contact model. The Hölzer-Sommerfeld drag model is used to represent the inter-phase drag force with considering particle shape and orientation. The integrated model is validated towards the discharge process in a hopper and the flow dynamics in a

BFB. After then, the general flow patterns, solid mixing, and solid dispersion are studied. The findings are expected to shed light on solid transportation mechanisms in this complicated flow system. Based on the results, the following tips can be drawn:

1) The discharge pattern in a hopper and flow pattern in a BFB are qualitatively and quantitatively predicted, demonstrating the reasonability of coupling the CFD-DEM approach with the super-quadric model. Minimum fluidization velocity increases with the aspect ratio. Bed permeability depends on the bed porosity and particle shape. Ellipsoid particles are easier to be hindered by the surrounding particles than spherical particles.
2) Bubbles place a significant role in determining flow patterns, which have a preferential path of the central region along with the bed height. A double-recirculation pattern in which particles mainly moves from the wall to the centre in the lower bed and oppositely in the upper bed are formed. The non-sphericity delays the fluidization of ellipsoid particles, at high superficial gas velocities, the solid circulation is qualitatively similar to that of the spherical particles. Ellpsoid particles with lower sphericity (i.e., AR = 0.5, 2.0) form more "bridges" around the bubbles, which hinder the bed permeability and particle motions.
3) The mixing process includes three stages: the unsteady start-up state, the vigorous mixing state, and the final steady state. The first stage is the foundation while the second stage driven by bubble dynamics dominates the whole mixing process in the bed. The convective mixing and shear mixing is significant to establish the "coarse mixing stage", while the diffusive mixing accomplishes the "fine mixing stage" to make the system approach the equilibrium state. Lacey mixing index is used to quantify the mixing degree, in which the mixing quality is insensitive to the sampling grid size when sufficient samples are provided. Ellipsoid particles with higher sphericity (e.g., AR = 0.75 and 1.5) show a lower mixing performance in the bed.
4) The magnitude of the *Dx*, *Dy*, and *Dz* is about ~10^{-3} m^2/s, ~10^{-5} m^2/s, and ~10^{-2} m^2/s, respectively. The solid transportation intensity along with the bed depth is the smallest due to the restriction of the front and rear walls. The solid axial transportation intensity is the largest due to the introduction of vigorous airflow. Ellipsoid particles with higher sphericity (e.g., AR = 0.75 and 1.5) show larger solid dispersion intensity. The solid dispersion coefficient along with the axal direction is one order of magnitude larger than that along with the horizontal direction.

Credit author statement

- Research motivation: Wentao Zhang
- Data post-processing: Shiliang Yang
- Paper writing (Draft): Shiliang Yang
- Paper reviewing&editing: Wentao Zhang

Declaration of Competing Interest

The authors declare that they have no known competing financial interests or personal relationships that could have appeared to influence the work reported in this paper.

Acknowledgments

The financial support from the Applied Basic Research Project of Yunnan Province, China (No. 202001AU070030) is sincerely acknowledged.

References

[1] J. Azmir, Q. Hou, A. Yu, Discrete particle simulation of food grain drying in a fluidised bed, Powder Technol. 323 (2018) 238–249.
[2] Z. Duan, S. Sun, Z. Lan, Y. Wang, J. Zhang, J. Wang, Numerical simulation of a novel fluidized bed for gas-solid non-catalytic reactions (NRFB), Powder Technol. 372 (2020) 428–437.
[3] S. Wang, K. Luo, C. Hu, L. Sun, J. Fan, Impact of operating parameters on biomass gasification in a fluidized bed reactor: an Eulerian-Lagrangian approach, Powder Technol. 333 (2018) 304–316.
[4] C. Hu, K. Luo, S. Wang, L. Sun, J. Fan, Influences of operating parameters on the fluidized bed coal gasification process: a coarse-grained CFD-DEM study, Chem. Eng. Sci. 195 (2019) 693–706.
[5] N. Gui, J. Fan, Numerical study of particle mixing in bubbling fluidized beds based on fractal and entropy analysis, Chem. Eng. Sci. 66 (12) (2011) 2788–2797.
[6] K.A. Buist, P. Jayaprakash, J. Kuipers, N.G. Deen, J.T. Padding, Magnetic particle tracking for nonspherical particles in a cylindrical fluidized bed, AICHE J. 63 (12) (2017) 5335–5342.
[7] V.V. Mahajan, J.T. Padding, T.M. Nijssen, K.A. Buist, J. Kuipers, Nonspherical particles in a pseudo-2D fluidized bed: experimental study, AICHE J. 64 (5) (2018) 1573–1590.
[8] B.W. Fitzgerald, A. Zarghami, V.V. Mahajan, S.K.P. Sanjeevi, I. Mema, V. Verma, et al., Multiscale simulation of elongated particles in fluidised beds, Chem. Eng. Sci. X 2 (2019) 100019.
[9] S. Wang, K. Luo, C. Hu, J. Fan, CFD-DEM study of the effect of cyclone arrangements on the gas-solid flow dynamics in the full-loop circulating fluidized bed, Chem. Eng. Sci. 172 (2017) 199–215.
[10] S. Wang, K. Luo, S. Yang, C. Hu, J. Fan, Parallel LES-DEM simulation of dense flows in fluidized beds, Appl. Therm. Eng. 111 (2017) 1523–1535.
[11] K. Luo, F. Wu, S. Yang, J. Fan, CFD–DEM study of mixing and dispersion behaviors of solid phase in a bubbling fluidized bed, Powder Technol. 274 (2015) 482–493.
[12] M.A. van der Hoef, Annaland M. van Sint, N.G. Deen, J. Kuipers, Numerical simulation of dense gas-solid fluidized beds: a multiscale modeling strategy, Annu. Rev. Fluid Mech. 40 (2008) 47–70.
[13] G. Lu, J.R. Third, C.R. Müller, Discrete element models for non-spherical particle systems: from theoretical developments to applications, Chem. Eng. Sci. 127 (2015) 425–465.
[14] M.J. Rhodes, X.S. Wang, M. Nguyen, P. Stewart, K. Liffman, Study of mixing in gas-fluidized beds using a DEM model, Chem. Eng. Sci. 56 (8) (2001) 2859–2866.
[15] A. Di Renzo, F.P. Di Maio, R. Girimonte, B. Formisani, DEM simulation of the mixing equilibrium in fluidized beds of two solids differing in density, Powder Technol. 184 (2) (2008) 214–223.
[16] D. Liu, X. Chen, Lateral solids dispersion coefficient in large-scale fluidized beds, Combust. Flame 157 (11) (2010) 2116–2124.
[17] H.R. Norouzi, N. Mostoufi, Z. Mansourpour, R. Sotudeh-Gharebagh, J. Chaouki, Characterization of solids mixing patterns in bubbling fluidized beds, Chem. Eng. Res. Des. 89 (6) (2011) 817–826.
[18] W. Zhong, A. Yu, X. Liu, Z. Tong, H. Zhang, DEM/CFD-DEM modelling of non-spherical particulate systems: theoretical developments and applications, Powder Technol. 302 (2016) 108–152.
[19] S. Shrestha, S. Kuang, A. Yu, Z. Zhou, Bubble dynamics in bubbling fluidized beds of ellipsoidal particles, AIChE J. 65 (11) (2019).
[20] B. Ren, W. Zhong, Y. Chen, X. Chen, B. Jin, Z. Yuan, et al., CFD-DEM simulation of spouting of corn-shaped particles, Particuology 10 (5) (2012) 562–572.
[21] T. Oschmann, J. Hold, H. Kruggel-Emden, Numerical investigation of mixing and orientation of non-spherical particles in a model type fluidized bed, Powder Technol. 258 (2014) 304–323.
[22] K. Vollmari, T. Oschmann, H. Kruggel-Emden, Mixing quality in mono- and bidisperse systems under the influence of particle shape: a numerical and experimental study, Powder Technol. 308 (2017) 101–113.
[23] E. Abbaszadeh Molaei, A.B. Yu, Z.Y. Zhou, Particle scale modelling of mixing of ellipsoids and spheres in gas-fluidized beds by a modified drag correlation, Powder Technol. 343 (2019) 619–628.
[24] H. Ma, Y. Zhao, Investigating the fluidization of disk-like particles in a fluidized bed using CFD-DEM simulation, Adv. Powder Technol. 29 (10) (2018) 2380–2393.
[25] I. Mema, J.T. Padding, Spherical versus elongated particles - numerical investigation of mixing characteristics in a gas fluidized bed, Chem. Eng. Sci. X 8 (2020) 100079.
[26] V.V. Mahajan, T.M.J. Nijssen, J.A.M. Kuipers, J.T. Padding, Non-spherical particles in a pseudo-2D fluidised bed: modelling study, Chem. Eng. Sci. 192 (2018) 1105–1123.
[27] Z. Wang, M. Liu, X. Yang, A four-way coupled CFD-DEM modeling framework for charged particles under electrical field with applications to gas insulated switchgears, Powder Technol. 373 (2020) 433–445.
[28] R. Liu, Z. Zhou, R. Xiao, A. Yu, CFD-DEM modelling of mixing of granular materials in multiple jets fluidized beds, Powder Technol. 361 (2020) 315–325.
[29] A. Podlozhnyuk, S. Pirker, C. Kloss, Efficient implementation of superquadric particles in Discrete Element Method within an open-source framework, Comput. Part. Mech. 4 (1) (2017) 101–118.
[30] J. Gan, Z. Zhou, A. Yu, Particle scale study of heat transfer in packed and fluidized beds of ellipsoidal particles, Chem. Eng. Sci. 144 (2016) 201–215.
[31] H. Ma, L. Xu, Y. Zhao, CFD-DEM simulation of fluidization of rod-like particles in a fluidized bed, Powder Technol. 314 (2017) 355–366.
[32] A. Hölzer, M. Sommerfeld, New simple correlation formula for the drag coefficient of non-spherical particles, Powder Technol. 184 (3) (2008) 361–365.
[33] S.B. Kuang, A.B. Yu, Micromechanic modeling and analysis of the flow regimes in horizontal pneumatic conveying, AIChE J. 57 (10) (2011) 2708–2725.
[34] M. Saidi, H. Basirat Tabrizi, J.R. Grace, C.J. Lim, G. Ahmadi, Hydrodynamic and mixing characteristics of gas-solid flow in a pulsed spouted bed, Ind. Eng. Chem. Res. 54 (32) (2015) 7933–7941.
[35] S. Shrestha, S.B. Kuang, A.B. Yu, Z.Y. Zhou, Orientation of spheroidal particles in single jet bubbling fluidized beds, Powder Technol. 361 (2020) 363–373.

[36] X. Gao, J. Yu, L. Lu, C. Li, W.A. Rogers, Development and validation of SuperDEM-CFD coupled model for simulating non-spherical particles hydrodynamics in fluidized beds, Chem. Eng. J. 420 (2021) 127654.
[37] B. Soltanbeigi, A. Podlozhnyuk, S. Papanicolopulos, C. Kloss, S. Pirker, J.Y. Ooi, DEM study of mechanical characteristics of multi-spherical and superquadric particles at micro and macro scales, Powder Technol. 329 (2018) 288–303.
[38] P.A. Cundall, O.D. Strack, A discrete numerical model for granular assemblies, Geotechnique 29 (1) (1979) 47–65.
[39] H.P. Zhu, Z.Y. Zhou, R.Y. Yang, A.B. Yu, Discrete particle simulation of particulate systems: theoretical developments, Chem. Eng. Sci. 62 (13) (2007) 3378–3396.
[40] R. Di Felice, The voidage function for fluid-particle interaction systems, Int. J. Multiphase Flow 20 (1) (1994) 153–159.
[41] G.H. Ganser, A rational approach to drag prediction of spherical and nonspherical particles, Powder Technol. 77 (2) (1993) 143–152.
[42] D.A. Clarke, A.J. Sederman, L.F. Gladden, D.J. Holland, Investigation of void fraction schemes for use with CFD-DEM simulations of fluidized beds, Ind. Eng. Chem. Res. 57 (8) (2018) 3002–3013.
[43] J.H. Ferziger, M. Peric, Computational Methods for Fluid Dynamics, Springer Science & Business Media, 2012.
[44] R.I. Issa, Solution of the implicitly discretised fluid flow equations by operator-splitting, J. Comput. Phys. 62 (1) (1986) 40–65.
[45] Y. Tsuji, T. Kawaguchi, T. Tanaka, Discrete particle simulation of two-dimensional fluidized bed, Powder Technol. 77 (1) (1993) 79–87.
[46] S. Yang, K. Luo, J. Fan, K. Cen, Particle-scale investigation of the solid dispersion and residence properties in a 3-D spout-fluid bed, AICHE J. 60 (8) (2014) 2788–2804.
[47] X. Chen, W. Zhong, X. Zhou, B. Jin, B. Sun, CFD–DEM simulation of particle transport and deposition in pulmonary airway, Powder Technol. 228 (2012) 309–318.
[48] A. Hobbs, Simulation of an aggregate dryer using coupled CFD and DEM methods, Int. J. Comput. Fluid D 23 (2) (2009) 199–207.
[49] Y. Shao, X. Liu, W. Zhong, B.S. Jin, M. Zhang, Recent advances of spout-fluid bed: a review of fundamentals and applications, Int. J. Chem. React. Eng. 11 (1) (2013) 243–258.
[50] S.D. Liu, Z.Y. Zhou, R.P. Zou, D. Pinson, A.B. Yu, Flow characteristics and discharge rate of ellipsoidal particles in a flat bottom hopper, Powder Technol. 253 (2014) 70–79.
[51] C.R. Müller, D.J. Holland, A.J. Sederman, S.A. Scott, J.S. Dennis, L.F. Gladden, Granular temperature: comparison of magnetic resonance measurements with discrete element model simulations, Powder Technol. 184 (2) (2008) 241–253.
[52] W. Nan, Y. Wang, J. Wang, Numerical analysis on the fluidization dynamics of rod-like particles, Adv. Powder Technol. 27 (5) (2016) 2265–2276.
[53] P.M.C. Lacey, Developments in the theory of particle mixing, J. Appl. Chem. 4 (5) (1954) 257–268.
[54] M. Fang, K. Luo, S. Yang, K. Zhang, J. Fan, Computational fluid dynamics-discrete element method investigation of solid mixing characteristics in an internally circulating fluidized bed, Ind. Eng. Chem. Res. 52 (22) (2013) 7556–7568.
[55] R.W. Breault, A review of gas–solid dispersion and mass transfer coefficient correlations in circulating fluidized beds, Powder Technol. 163 (1–2) (2006) 9–17.
[56] J. Sánchez-Prieto, F. Hernández-Jiménez, L.M. Garcia-Gutierrez, A. Soria-Verdugo, Experimental study on the characteristic mixing time of solids and its link with the lateral dispersion coefficient in bubbling fluidized beds, Chem. Eng. J. 307 (2017) 113–121.